Chapter 5

Partially insulated cracks in orthotropic materials under steady state thermo-mechanical loadings

5.1 Introduction

5.1.1 Background

Composite materials have gained tremendous attention due to their improved physical properties, such as high strength and lightness, and their applications in various engineering structures. The disparity in thermal properties between adjacent materials predominantly induces cracks at the interface. This type of fracture becomes especially hazardous in an essential thermal field. A crack that forms between dissimilar materials when subjected to thermal and mechanical loadings presents a significant challenge in composite structures. For this reason, it is necessary to examine cracks subjected to thermo-mechanical loading to improve the selection of materials and fabrication techniques that will not result in material breakage. They cause additional disturbances of stress components and weaken the material under force and thermal factors. Critical areas of interest include the concentration of thermal stress near the ends of cracks and opening displacements of cracks. By investigating the thermoelastic field surrounding fractures, the stability and service life of fractured engineering materials and structures can be better understood [26, 69]. The partially insulated crack model is stated as

$$q_c = -h_c \, \Delta T, \tag{5.1}$$

where q_c, h_c and ΔT are the heat flux, thermal conductivity coefficient through the crack region, and the temperature difference between the crack faces, respectively. The limiting values $h_c = 0$ or $h_c \to \infty$ represent a fully thermally impermeable or permeable crack. The crack-face thermal boundary equation mentioned in equation (5.1) has been widely used [131, 132, 133].

In the research article, [134] investigated that heat flux exhibits squared root singularity in interface cracks. In the polar form (r, T), the asymptotic expression of heat flux near the crack tip $x = a$ is given by

$$q_y = \frac{K_H}{\sqrt{2r}}\sqrt{a}\,\cos(T/2), q_x = -\frac{K_H}{\sqrt{2r}}\sqrt{a}\,\sin(T/2). \tag{5.2}$$

HFIF is a parameter that characterises the strength of thermal energy in the medium. HFIF is a physical parameter introduced to measure and quantify the thermal energy intensification in the vicinity of the crack tip. Other parameters, normalised crack displacements are crucial fracture criterion that precedes material failure since

the crack faces experience displacement while experiencing deformations. Crack displacements have been categorised as COD in the $y-$ direction and CSD given in the $x-$ direction.
However, for a wider practical purpose and to improve the applicability of the problem, a deep investigation of cracks under the impact of some thermal conductivity of their own is required.

Overall, this study paves the way for a deeper understanding of the complexities inherent in composite mediums and offers valuable contributions to this intriguing field of research.

5.1.2 Literature survey and research gaps

Based on the theory of thermoelasticity [69], considerable efforts have been devoted to analysing a solid. An investigation into the nature of thermal stress singularities at the crack tip in a transversely isotropic solid was conducted by Sih [55]. As indicated by his observations, the local singularities of thermal stresses near the point of a fracture are identical to those of mechanical stresses. A study on the thermal stresses of an anisotropic plate has been done in [135, 136]. The article [137] analyses an interface crack characterised by partially insulated crack surfaces in an isotropic material subjected to a heat flow. An analogous issue was investigated in [138], albeit with the inclusion of a heat transmission coefficient between the crack surfaces. The article [139] determined the SIFs for an insulated and partially insulated interface fracture in an isotropic material subject to heat flow. The study investigated the effect of micro defects on an interface fracture in a material subjected to a heat flux. Tsai [54] investigated orthotropic materials under uniform heat flow. Insulated or isothermal crack problems neglect the thermal conductivity of any medium inside the crack faces. Due to the presence of cracks, there are discontinuities in the temperature and displacements, but based on the assumption that the medium trapped inside the cracks can conduct some heat within it provides a more realistic approach to the problems of thermoelasticity. A study of fully insulated cracks in orthotropic composite medium has been done in [7]. [140] by using the finite element alternating method (FEM) to calculate the temperature distribution on a finite plate with insulated cracks under steady-state conditions. Similarly, [141] undertook a study using the boundary element alternating method (BEM). The FEM stands out as a robust numerical tool for thermal fracture analysis, but it is worth noting that the accuracy of the FEM solution is significantly influenced by the mesh employed. Specifically, both FEM and BEM can efficiently yield numerical solutions for uncracked finite bodies using a coarser mesh. Further, the present study has been validated by the explicit form of the solution provided by [8].

In contrast to previous research concerning the thermoelastic analysis of a cracked solid, the effects of applied mechanical loads and thermal conductivity of the crack interior on the thermal SIF can be accounted for using the relevant boundary conditions for the thermal medium model implemented by [6]. Similarly, the intensity factors of thermal stress have been consistently computed to define the thermal stress field. [142] determined that by applying a uniform heat flow, a crack produces the mode-II SIF. In recent times, many research works have been dedicated to studying stress problems orthotropic materials with finite or semi-infinite cracks using various approaches [143, 144, 145]. The novel aspects and the objectives of the study are encapsulated as follows

- An investigation has been conducted to examine the multiple thermally conducting cracks in dissimilar orthotropic composite mediums. This study investigates the relationship between the thermal conductivity coefficient and various parameters of heat flux, stresses and temperatures in detail.

- The Schmidt method [146] has been used in this study, which involves using polynomials expansion [138] of the temperature and displacement jumps at the interface. This approach is novel for such types of problems and is employed to solve the integral equations and derive the approximate solutions for the considered problem.

- The detailed analysis and computation of expressions for various physical parameters viz., HFIF, SIFs for mode-I and mode-II cracks, and crack displacements have been determined by semi-analytical and numerical techniques for the considered problem.

- Graphical comparisons and validation have been carried out to facilitate a comparative analysis of the results obtained in the present study with the existing results given in [8, 6] for particular cases.

- For various particular cases, graphs have been plotted to illustrate the numerical results and showcase the interrelations between crack lengths, bonded strip width, and the partial conductivity coefficient of the crack surface in a more effective manner.

5.1.3 Chapter organisation

In the present chapter, an attempt has been made to study the partially insulated interfacial cracks in the orthotropic composite medium for the considered material choices and to analyse the dependency of the thermal conductivity coefficient on different parameters HFIF, SIF, COD and CSD. Section 5.2 contains the concerned governing equations and problem formulation. The geometry of the problem has been discussed with the boundary and continuity conditions. Section 5.3 contains the solution procedure, which is based on Chebyshev-like polynomial expansion of temperature and displacement differences, which is employed to solve the integral equations and obtain approximate solutions for the problem. The integral equations are converted into systems of algebraic equations given in sub-sections 5.3.1 and 5.3.2, and the problem is reduced to finding unknown coefficients. Under the assumptions of partially insulated crack surface, the corresponding mixed boundary value problem is transformed into solving singular integral equations with the help of Fourier integral transformation. Finally, the semi-analytical solutions for the HFIF, mode-I and mode-II type SIFs, COD, and CSD at all the crack tips under thermoelastic loading are obtained in sub-section 5.3.3. Section 5.4 contains the numerical solutions of the parameters that have been calculated semi-analytically and depicted graphically using particular material choices for numerical calculations. These successfully represent the dependent nature of crack lengths, strip width, and thermal conduction coefficient. Comparative studies have been shown graphically between the present study and previous research to analyse the chapter's methods.

5.2 Mathematical formulation of the problem

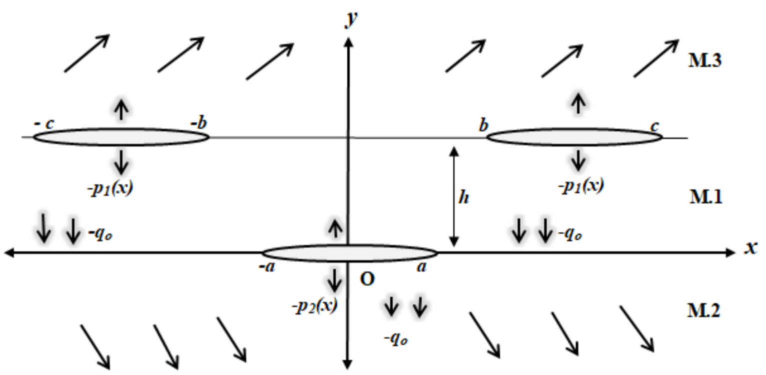

FIGURE 5.1: Geometry of the partially insulated crack model under uniform heat flux and mechanical loading in orthotropic medium.

Consider a semi-infinite orthotropic strip of depth h bonded between two orthotropic half-planes at $y = 0$ and $y = h$ as shown in Figure 5.1. The mathematical model consists of one central crack of length $2a$ $(-a < x < a, y = 0)$ along with two collinear cracks $(b < |x| < c,\ y = h)$ situated at the upper interface. The system is subjected to steady-state heat flux q_0 flowing in a negative y-direction and tensile mechanical loads $p_1(x),\ p_2(x)$. Here, a negative sign is used to denote the tensile. The superscripts $(i) = 1,\ 2,\ 3$ depict the three orthotropic media viz. M.1, M.2, and M.3, respectively, as shown in Figure 5.1. Based on the theory of linear thermoelasticity and using the equations (2.1)-(2.4) the temperature field $T(x, y)$ is expressed as

$$\hat{T}^{(1)}(s, y) = A_1(s)\ \cosh\big(sk^{(1)}y\big) + A_2(s)\ \sinh\big(sk^{(1)}y\big), \tag{5.3}$$

$$\hat{T}^{(2)}(s, y) = B_1(s)\ e^{sk^{(2)}y}, \tag{5.4}$$

$$\hat{T}^{(3)}(s, y) = C_1(s)\ e^{-sk^{(3)}y}, \tag{5.5}$$

where the unknown functions $A_j's,\ B_1,\ C_1,$ of transformed variable s, are to be determined to obtain the complete temperature field.

Tensile and shear stress components are related to displacements as mentioned in sub-section 2.2.2.

The general expressions for displacements with isothermal and non-isothermal terms are obtained in a similar manner as given in [101]. Next, by using the equations

(2.10)-(2.12) as

$$\hat{\sigma}^{(1)}_{yy}(s,y) = s\ a_{11}\ D_1(s)\ \cosh\left(s\alpha^{(1)}_1 y\right) + s\ a_{11}\ D_2(s)\ \sinh\left(s\alpha^{(1)}_1 y\right) + s\ a_{12}\ D_3(s)$$
$$\cosh\left(s\alpha^{(1)}_2 y\right) + s\ a_{12}\ D_4(s)\ \sinh\left(s\alpha^{(1)}_2 y\right) + b_1\ A_1(s)\ \cosh\left(sk^{(1)}y\right)$$
$$+ b_1\ A_2(s)\ \sinh\left(sk^{(1)}y\right), \tag{5.6}$$

$$\hat{\sigma}^{(2)}_{yy}(s,y) = a_{21}\ s\ E_1(s)\ e^{s\alpha^{(2)}_1 y} + s\ a_{22}\ E_2(s)\ e^{s\alpha^{(2)}_2 y} + b_2\ B_1(s)\ e^{sk^{(2)}y}, \tag{5.7}$$

$$\hat{\sigma}^{(3)}_{yy}(s,y) = s\ a_{31}\ F_1(s)\ e^{-s\alpha^{(3)}_1 y} + s\ a_{32}\ F_2(s)\ e^{-s\alpha^{(3)}_2 y} + b_3\ C_1\ e^{-sk^{(3)}y}, \tag{5.8}$$

$$\bar{\sigma}^{(1)}_{xy}(s,y) = s\ C_{11}\ D_1\ \sinh\left(s\alpha^{(1)}_1 y\right) + s\ C_{11}\ D_2\ \cosh\left(s\alpha^{(1)}_1 y\right) + s\ C_{12}\ D_3\ \sinh\left(s\alpha^{(1)}_2 y\right)$$
$$+ s\ C_{12}\ D_4\ \cosh\left(s\alpha^{(1)}_2 y\right) + d_1\ A_1\ \sinh\left(sk^{(1)}y\right) + d_1\ A_2\ \cosh\left(sk^{(1)}y\right), \tag{5.9}$$

$$\bar{\sigma}^{(2)}_{xy}(s,y) = c_{21}\ s\ E_1(s)\ e^{s\alpha^{(2)}_1 y} + s\ c_{22}\ E_2(s)\ e^{s\alpha^{(2)}_2 y} + d_2\ B_1(s)\ e^{sk^{(2)}y}, \tag{5.10}$$

$$\bar{\sigma}^{(3)}_{xy}(s,y) = -\ s\ c_{31}\ F_1(s)\ e^{-s\alpha^{(3)}_1 y} - s\ c_{32}\ F_2(s)\ e^{-s\alpha^{(3)}_2 y} - d_3\ C_1\ e^{-sk^{(3)}y}, \tag{5.11}$$

where $D_j,\ E_j,\ F_j\ 's$ are all unknown coefficients to be determined using prescribed stress and displacement boundary conditions, $\bar{\sigma}$ denotes the Fourier sine transform equation (1.28b) and

$$\begin{aligned} a_{ij} &= C^{(i)}_{12} - \alpha^{(i)}_j\ \gamma^{(i)}_j\ C^{(i)}_{22}, \qquad & b_i &= C^{(i)}_{12}\ \eta^{(i)}_1\ + C^{(i)}_{22}\ \eta^{(i)}_1\ k^{(i)}\ - \beta^{(i)}_2, \\ c_{ij} &= C^{(i)}_{66}\ (\alpha^{(i)}_j + \gamma^{(i)}_j), & d_i &= Q^{(i)}_{66}\ (\eta^{(i)}_1 k^{(i)} - \eta^{(i)}_2). \end{aligned} \tag{5.12}$$

In the present chapter, thermo-mechanical loadings are applied on the crack surfaces. The heat flux flow is in a negative $y-$ direction, and the tensile mechanical load is taken with the '-' sign. The corresponding conditions for the partially insulated crack model are

$$k_y^{(1)}\ \frac{\partial T^{(1)}(x,h)}{\partial y} = k_y^{(3)}\ \frac{\partial T^{(3)}(x,h)}{\partial y} = -(q_o - q_{oc}) \quad , \quad b < x < c, \tag{5.13}$$

$$k_y^{(1)}\ \frac{\partial T^{(1)}(x,0)}{\partial y} = k_y^{(2)}\ \frac{\partial T^{(2)}(x,h)}{\partial y} = -(q_o - q_{oc}) \quad , \quad 0 < x < a, \tag{5.14}$$

$$\sigma_{yy}^{(1)}(x,h) = -p_1(x), \quad \sigma_{xy}^{(1)}(x,h) = 0 \ \ , \ \ b < x < c, \tag{5.15}$$

$$\sigma_{yy}^{(1)}(x,0) = -p_2(x), \quad \sigma_{xy}^{(1)}(x,0) = 0 \ \ , \ \ 0 < x < a, \tag{5.16}$$

$$T^{(j)}(x,y) = 0, \quad \sqrt{x^2+y^2} \to \infty, \ j = 2,3, \tag{5.17}$$

$$u^{(j)}(x,y) = 0, \quad v^{(j)}(x,y) = 0, \quad \sqrt{x^2+y^2} \to \infty, \ j = 2,3, \tag{5.18}$$

on the planes containing the cracks at $y = 0$ and $y = h$. Here $q_{oc} = -h_c\ \Delta T$ where h_c is the thermal conductivity inside the crack region, and ΔT is the temperature difference between the upper and lower parts of the crack. The extreme values $h_c = 0$ and $h_c = \infty$ represent the thermally insulated and thermally permeable crack, respectively [8]. The above equations contain terms induced by thermal flux q_0 and mechanical loadings $p_1,\ p_2$.

The continuity of temperature fields, heat fluxes, stress and displacement components gives the conditions for crack-free boundaries at $y = 0$ and $y = h$, which can be written as

$$q_y^{(3)}(x,h) = q_y^{(1)}(x,h), \quad q_y^{(1)}(x,0) = q_y^{(2)}(x,0), \quad 0 < x < \infty, \tag{5.19}$$

$$T^{(1)}(x,h) = T^{(3)}(x,h), \quad x < b, \; x > c, \tag{5.20}$$

$$T^{(1)}(x,0) = T^{(2)}(x,0), \quad x > a, \tag{5.21}$$

$$k_y^{(1)} \frac{\partial T^{(1)}(x,h)}{\partial y} = k_y^{(3)} \frac{\partial T^{(3)}(x,h)}{\partial y}, \quad x < b, \; x > c, \tag{5.22}$$

$$k_y^{(1)} \frac{\partial T^{(1)}(x,0)}{\partial y} = k_y^{(2)} \frac{\partial T^{(2)}(x,0)}{\partial y}, \quad x > a, \tag{5.23}$$

$$\sigma_{yy}^{(3)}(x,h) = \sigma_{yy}^{(1)}(x,h) \;\; , \;\; \sigma_{yy}^{(1)}(x,0) = \sigma_{yy}^{(2)}(x,0) \;\; , \;\; 0 < x < \infty, \tag{5.24}$$

$$\sigma_{xy}^{(3)}(x,h) = \sigma_{xy}^{(1)}(x,h) \;\; , \;\; \sigma_{xy}^{(1)}(x,0) = \sigma_{xy}^{(2)}(x,0) \;\; , \;\; 0 < x < \infty, \tag{5.25}$$

$$u^{(1)}(x,h) = u^{(3)}(x,h), \quad v^{(1)}(x,h) = v^{(3)}(x,h) \;\; , \;\; x < b, \; x > c, \tag{5.26}$$

$$u^{(1)}(x,0) = u^{(2)}(x,0), \quad v^{(1)}(x,0) = v^{(2)}(x,0) \;\; , \;\; x > a. \tag{5.27}$$

5.3 Solution procedure

The more conventional methods, such as the collocation technique, are based on introducing auxiliary functions to convert the dual integral problem to Cauchy-type singular integral equations. Here, a more direct numerical method of solving dual integrals is used. The Schmidt method is based on applying series expansion of temperature and displacements in the form of an orthogonal polynomial that can form a complete set. For this purpose, series expansion is done using Chebyshev-like polynomials [147]. The Schmidt method is usually a powerful tool used to solve a system of algebraic equations with unknown coefficients involving an orthogonal complete set of polynomials. It involves the procedure of building a solution by employing the orthogonality condition. Since the temperature field is free of any elastic strain, it can be solved independently first by substituting the jump in temperature across the crack surfaces as

$$\phi_1(x) = T^{(3)}(x,h) - T^{(1)}(x,h), \tag{5.28}$$

$$\phi_2(x) = T^{(1)}(x,0) - T^{(2)}(x,0). \tag{5.29}$$

By applying the Fourier transform and thermal boundary conditions, we get

$$\sqrt{\frac{2}{\pi}} \int_0^\infty \hat{\phi}_1(s)\ \cos(sx)\ ds = 0, \quad x < b,\ x > c, \tag{5.30}$$

$$\sqrt{\frac{2}{\pi}} \int_0^\infty \hat{\phi}_2(s)\ \cos(sx)\ ds = 0, \quad x > a. \tag{5.31}$$

Using integration properties given in [40] to the above equations, we obtain,

$$\hat{\phi}_1(s) = \sum_{n=1}^{\infty} a_n\ \frac{1}{s}\ \sin\left(x_o\ s - \frac{n\pi}{2}\right)\ J_n(l_o s), \tag{5.32}$$

$$\hat{\phi}_2(s) = \sum_{n=1}^{\infty} b_n\ \frac{2n-1}{s}\ J_{2n-1}(s\ a), \tag{5.33}$$

where $(c-b)/2 = l_o,\ (c+b)/2 = x_o$ and $J_n(x)$ is Bessels function. Using equations (5.32) and (5.33), the unknown functions ϕ_1 and ϕ_2 are obtained in form of Chebyshev-like polynomials as

$$\phi_1(x) = \sum_{n=0}^{\infty} a_n\ \frac{1}{\sqrt{2\pi}\ n}\ \sin\left(n\ \sin^{-1}\left(\frac{x_o - x}{l_o}\right) - \frac{n\pi}{2}\right), b < x < c, \tag{5.34}$$

$$\phi_2(x) = \sum_{n=1}^{\infty} b_n\ \frac{1}{\sqrt{2\pi}}\ \cos\left((2n-1)\ \sin^{-1}(\frac{x}{a})\right), 0 < x < a \tag{5.35}$$

(5.36)

In a similar manner, the stress and displacement boundary conditions (5.26) and (5.27) can be satisfied by writing the difference in displacements at $y = 0,\ y = h$ as [148]

$$u^{(3)}(x,h) - u^{(1)}(x,h) = \begin{cases} \sum_{n=1}^{\infty} c_n \frac{1}{\sqrt{2\pi}\ n}\ \sin\left(n \arcsin\left(\frac{x_o - x}{l_o}\right) - \frac{n\pi}{2}\right), & b < x < c \\ 0 & \text{, elsewhere,} \end{cases} \tag{5.37}$$

$$v^{(3)}(x,h) - v^{(1)}(x,h) = \begin{cases} \sum_{n=1}^{\infty} d_n \frac{1}{\sqrt{2\pi}\ n} \sin\left(n\ \arcsin\left(\frac{x_o - x}{l_o}\right) - \frac{n\pi}{2}\right), & b < x < c \\ 0 & \text{, elsewhere,} \end{cases} \tag{5.38}$$

$$u^{(1)}(x,0) - u^{(2)}(x,0) = \begin{cases} \sum_{n=1}^{\infty} e_n\ \frac{1}{\sqrt{2\pi}}\ \sin\left(2\ n\ \arcsin\left(\frac{-x}{a}\right)\right), & 0 < x < a \\ 0 & \text{, elsewhere,} \end{cases} \tag{5.39}$$

$$v^{(1)}(x,0) - v^{(2)}(x,0) = \begin{cases} \sum_{n=1}^{\infty} f_n\ \frac{1}{\sqrt{2\pi}}\ \cos\left((2n-1)\ \arcsin\left(\frac{x}{a}\right)\right), & 0 < x < a \\ 0 & \text{, elsewhere.} \end{cases} \tag{5.40}$$

The Fourier cosine transform is used to solve integrals in the models under the condition that the source term is even in x, and the Fourier sine transform is used for odd function terms. The expressions for the equations (5.37)-(5.40) in the transformed domain in the form of infinite series involving Bessel functions are given by

$$(-1)\ (\bar{u}^{(3)}(s,h) - \bar{u}^{(1)}(s,h)) = \sum_{n=1}^{\infty} c_n\ \frac{1}{s}\ \cos\left(x_o\ s - \frac{n\pi}{2}\right)\ J_n(l_o s), \tag{5.41}$$

$$\hat{v}^{(3)}(s,h) - \hat{v}^{(1)}(s,h) = \sum_{n=1}^{\infty} d_n\ \frac{1}{s}\ \sin\left(x_o\ s - \frac{n\pi}{2}\right)\ J_n(l_o s), \tag{5.42}$$

$$(-1)\ (\bar{u}^{(1)}(s,0) - \bar{u}^{(2)}(s,0)) = \sum_{n=1}^{\infty} e_n\ \frac{2n}{s}\ J_{2n}(s\ a), \tag{5.43}$$

$$\hat{v}^{(1)}(s,0) - \hat{v}^{(2)}(s,0) = \sum_{n=1}^{\infty} f_n\ \frac{2n-1}{s}\ J_{2n-1}(s\ a). \tag{5.44}$$

Using the above substitutions, the given problem is now reduced to find expansion coefficient terms $a_n,\ b_n,\ c_n,\ d_n,\ e_n,\ f_n$ using the principle of orthogonalisation. To proceed further, we use the thermal and traction conditions given in equations (5.13)-(5.16). The main benefit of this method is that achieving maximum efficiency in forming linear equations will result in a better solution for the problem [149].

5.3.1 Temperature field

Applying the thermal continuity conditions given in equations (5.19), we can reduce four unknown coefficients in equations (5.3)-(5.5) in the form of two unknowns, and we get

$$B_1 = \frac{\mu^{(1)}}{\mu^{(2)}} A_2, \quad C_1 = \frac{-\mu^{(1)}}{\mu^{(3)}}\ e^{sk^{(1)}h}\ (A_1\ \sinh\big(sk^{(1)}h\big) + A_2\ \cosh\big(sk^{(1)}h\big)). \tag{5.45}$$

By using the Fourier transformed expressions, the temperature difference across the interfaces with the boundary conditions given in equation (5.13) and (5.14) are obtained as dual integral equations for thermal loading. Thus, the temperature problem is now denoted by unknowns $a_n,\ b_n$. The integrands involved in the integral equations should decrease rapidly, and therefore, those are replaced in the modified forms as

$$\sum_{n=1}^{\infty} a_n \Bigg(\int_0^{\infty} (g_1(s)-\beta_1)\ \sin\left(x_o\ s - \frac{n\pi}{2}\right)\ J_n(l_o s)\ \cos(sx)\ ds + \beta_1\ t_n(x) \Bigg)$$
$$+ \sum_{n=1}^{\infty} b_n \int_0^{\infty} g_2(s)\ (2n-1)\ J_{2n-1}(sa)\ \cos(sx)\ ds = -\sqrt{\frac{\pi}{2}} \frac{(q_o - q_{oc})}{\mu^{(1)}} \quad , \quad b \le x \le c, \tag{5.46}$$

$$\sum_{n=1}^{\infty} a_n \int_0^{\infty} g_3(s)\ \sin\left(x_o\ s - \frac{n\pi}{2}\right)\ J_n(l_o s)\ \cos(sx)\ ds + \sum_{n=1}^{\infty} b_n \Bigg(\beta_4 \frac{\cos\left((2n-1)\ \sin^{-1}(\frac{x}{a})\right)}{\sqrt{a^2 - x^2}}$$
$$+ (2n-1) \int_0^{\infty} (g_4(s)-\beta_4)\ J_{2n-1}(sa)\ \cos(sx)\ ds \Bigg) = -\sqrt{\frac{\pi}{2}} \frac{(q_o - q_{oc})}{\mu^{(1)}} \quad , 0 \le x \le a, \tag{5.47}$$

where $\mu^{(i)} = \sqrt{k_y^{(i)} k_x^{(i)}}$ and

$$t_n(x) = (-1)^{\frac{n+1}{2}} \frac{1}{2} \left(\frac{l_o^n}{\sqrt{(x_o+x)^2 + (l_o)^2} \left(x_o + x + \sqrt{(x_o+x)^2 + (l_o)^2} \right)^n} + \frac{\cos\left(n\ \sin^{-1}(\frac{|x_o - x|}{l_o})\right)}{\sqrt{(l_o)^2 - (x_o - x)^2}} \right),$$

n is odd,

$$= (-1)^{\frac{n}{2}} \frac{1}{2} \left(\frac{l_o^n}{\sqrt{(x_o+x)^2 + (l_o)^2} \left(x_o + x + \sqrt{(x_o+x)^2 + (l_o)^2} \right)^n} + \frac{\sin\left(n\ \sin^{-1}(\frac{|x_o - x|}{l_o})\right)}{\sqrt{(l_o)^2 - (x_o - x)^2}} \right),$$

n is even, (5.48)

$$\lim_{s\to\infty} g_1(s) \to \beta_1 = \frac{\mu^{(3)}}{\mu^{(1)} + \mu^{(3)}}, \quad \lim_{s\to\infty} g_2(s) \to \beta_2 = 0, \tag{5.49}$$

$$\lim_{s\to\infty} g_3(s) \to \beta_3 = 0, \quad \lim_{s\to\infty} g_4(s) \to \beta_4 = \frac{\mu^{(2)}}{\mu^{(2)} + \mu^{(1)}}. \tag{5.50}$$

Thus, the system of algebraic equations for the temperature field obtained directly from equations (5.46) and (5.47) is given by

$$\sum_{n=1}^{\infty} a_n E_{1n}(x) + \sum_{n=1}^{\infty} b_n E_{2n}(x) = -h_{1n}(x), \quad b < x < c, \tag{5.51}$$

$$\sum_{n=1}^{\infty} a_n E_{3n}(x) + \sum_{n=1}^{\infty} b_n E_{4n}(x) = -h_{2n}(x), \quad 0 < x < a. \tag{5.52}$$

5.3.2 Stress and displacements

Applying the displacement continuity conditions in (5.24)-(5.27), we get

$$\begin{aligned} &s\,\Big(a_{11}\,\big(D_1(s)\,\cosh\big(s\alpha_1^{(1)}h\big) + D_2(s)\,\sinh\big(s\alpha_1^{(1)}h\big)\big) + a_{12}\,\big(D_3(s)\,\cosh\big(s\alpha_2^{(1)}h\big) \\ &+ D_4(s)\,\sinh\big(s\alpha_2^{(1)}h\big)\big) + a_{31}\,F_1(s)\,e^{-s\alpha_1^{(3)}h} + a_{32}\,F_2(s)\,e^{-s\alpha_2^{(3)}h}\Big) \\ &= -b_1\,\big(A_1(s)\,\cosh\big(sk^{(1)}h\big) + A_2(s)\,\sinh\big(sk^{(1)}h\big)\big) + b_3\,C_1(s)\,e^{-sk^{(3)}h}, \end{aligned} \tag{5.53}$$

$$s\,\Big(a_{11}\,D_1(s)\, + a_{12}\,D_3(s)\, - a_{21}\,E_1(s)\, - a_{22}\,E_2(s)\Big) = -b_1\,A_1(s) + b_2\,B_2(s)\,, \tag{5.54}$$

$$\begin{aligned} &s\,\Big(c_{11}\,\big(D_1(s)\,\sinh\big(s\alpha_1^{(1)}h\big) + D_2(s)\,\cosh\big(s\alpha_1^{(1)}h\big)\big) + c_{12}\,\big(D_3(s)\,\sinh\big(s\alpha_2^{(1)}h\big) \\ &+ D_4(s)\,\cosh\big(s\alpha_2^{(1)}h\big)\big) + c_{31}\,F_1(s)\,e^{-s\alpha_1^{(3)}h} + c_{32}F_2(s)\,e^{-s\alpha_2^{(3)}h}\Big) \\ &= -d_1\,\big(A_1(s)\,\sinh\big(sk^{(1)}h\big) + A_2(s)\,\cosh\big(sk^{(1)}h\big)\big) - d_3\,C_1(s)\,e^{-sk^{(3)}h}, \end{aligned} \tag{5.55}$$

$$s\,\Big(c_{11}\,D_2(s)\, + c_{12}\,D_4(s)\, - c_{21}\,E_1(s)\, - c_{22}\,E_2(s)\Big) = -d_1\,A_2(s)\, + d_2\,B_1(s)\,. \tag{5.56}$$

Further, a reduced system with four unknowns can be written in matrix form as

$$\begin{bmatrix} E_1 \\ E_2 \\ F_1 \\ F_2 \end{bmatrix} = \begin{bmatrix} e_{11} & e_{12} & e_{13} & e_{14} \\ e_{21} & e_{22} & e_{23} & e_{24} \\ e_{31} & e_{32} & e_{33} & e_{34} \\ e_{41} & e_{42} & e_{43} & e_{44} \end{bmatrix} \begin{bmatrix} D_1 \\ D_2 \\ D_3 \\ D_4 \end{bmatrix} + \frac{1}{s} \begin{bmatrix} e_{15} & e_{16} \\ e_{25} & e_{26} \\ e_{35} & e_{36} \\ e_{45} & e_{46} \end{bmatrix} \begin{bmatrix} A_1 \\ A_2 \end{bmatrix}, \tag{5.57}$$

where

$$e_{31} = e^{s\alpha_1^{(3)}h}\Big(f_1(s)\ \cosh\Big(s\alpha_1^{(1)}h\Big) + f_2(s)\ \sinh\Big(s\alpha_1^{(1)}h\Big)\Big), \tag{5.58a}$$

$$e_{32} = e^{s\alpha_1^{(3)}h}\Big(f_3(s)\ \cosh\Big(s\alpha_1^{(1)}h\Big) + f_4(s)\ \sinh\Big(s\alpha_1^{(1)}h\Big)\Big), \tag{5.58b}$$

$$e_{33} = e^{s\alpha_1^{(3)}h}\Big(f_5(s)\ \cosh\Big(s\alpha_2^{(1)}h\Big) + f_6(s)\ \sinh\Big(s\alpha_2^{(1)}h\Big)\Big), \tag{5.58c}$$

$$e_{34} = e^{s\alpha_1^{(3)}h}\Big(f_7(s)\ \cosh\Big(s\alpha_2^{(1)}h\Big) + f_8(s)\ \sinh\Big(s\alpha_2^{(1)}h\Big)\Big), \tag{5.58d}$$

$$e_{35} = e^{s\alpha_1^{(3)}h}\big(f_9(s)\ \cosh\big(sk^{(1)}h\big) + f_{10}(s)\ \sinh\big(sk^{(1)}h\big)\big), \tag{5.58e}$$

$$e_{36} = e^{s\alpha_1^{(3)}h}\big(f_{11}\cosh\big(sk^{(1)}h\big) + f_{12}\sinh\big(sk^{(1)}h\big)\big), \tag{5.58f}$$

$$e_{41} = e^{s\alpha_2^{(3)}h}\Big(f'_1(s)\ \cosh\Big(s\alpha_1^{(1)}h\Big) + f'_2(s)\ \sinh\Big(s\alpha_1^{(1)}h\Big)\Big), \tag{5.58g}$$

$$e_{42} = e^{s\alpha_2^{(3)}h}\Big(f'_3(s)\ \cosh\Big(s\alpha_1^{(1)}h\Big) + f'_4(s)\ \sinh\Big(s\alpha_1^{(1)}h\Big)\Big), \tag{5.58h}$$

$$e_{43} = e^{s\alpha_2^{(3)}h}\Big(f'_5(s)\ \cosh\Big(s\alpha_2^{(1)}h\Big) + f'_6(s)\ \sinh\Big(s\alpha_2^{(1)}h\Big)\Big), \tag{5.58i}$$

$$e_{44} = e^{s\alpha_2^{(3)}h}\Big(f'_7(s)\ \cosh\Big(s\alpha_2^{(1)}h\Big) + f'_8(s)\ \sinh\Big(s\alpha_2^{(1)}h\Big)\Big), \tag{5.58j}$$

$$e_{45} = e^{s\alpha_2^{(3)}h}\left(f'_9(s)\ \cosh\left(sk^{(1)}h\right) + f'_{10}(s)\ \sinh\left(sk^{(1)}h\right)\right), \tag{5.58k}$$

$$e_{46} = e^{s\alpha_2^{(3)}h}\left(f'_{11}\cosh\left(sk^{(1)}h\right) + f'_{12}\sinh\left(sk^{(1)}h\right)\right). \tag{5.58l}$$

Using the above substitution into the displacement equations given in (5.37)- (5.40), we get the system of equations as

$$\begin{bmatrix} l_{11} & l_{12} & l_{13} & l_{14} \\ l_{21} & l_{22} & l_{23} & l_{24} \\ l_{31} & l_{32} & l_{33} & l_{34} \\ l_{41} & l_{42} & l_{43} & l_{44} \end{bmatrix} \begin{bmatrix} D_1 \\ D_2 \\ D_3 \\ D_4 \end{bmatrix} + \frac{1}{s} \begin{bmatrix} l_{15} & l_{16} \\ l_{25} & l_{26} \\ l_{35} & l_{36} \\ l_{45} & l_{46} \end{bmatrix} \begin{bmatrix} A_1 \\ A_2 \end{bmatrix} = \begin{bmatrix} \sum_{n=1}^{\infty} c_n \frac{1}{s} \cos\left(x_o\ s - \frac{n\pi}{2}\right) J_n(l_o s) \\ \sum_{n=1}^{\infty} d_n \frac{1}{s} \sin\left(x_o s - \frac{n\pi}{2}\right) J_n(l_o s) \\ \sum_{n=1}^{\infty} e_n \frac{2n}{s} J_{2n}(sa) \\ \sum f_n \frac{(2n-1)}{s} J_{2n-1}(sa) \end{bmatrix}, \tag{5.59}$$

where $l_{ij}(s)$ are functions of $e_{ij}(s),\ f_i(s),\ f'_i(s)$ which are all known functions of $a_{ij},\ b_i,\ c_{ij},\ d_i$. Solving the unknowns in the form of right-hand side terms, all the terms in equations (5.6)-(5.11) can be written in the form of $c_n,\ d_n,\ e_n,\ f_n$. By using the Fourier transformed expressions of the displacement difference across the interfaces with the boundary conditions given in equations (5.15), (5.16), (5.24) and (5.25) we obtain four integral equations for tensile loading. Thus, the problem of stresses is now denoted by unknowns $c_n,\ d_n,\ e_n,\ f_n$. The integrands involved in the integral equations should decrease rapidly and are reduced in the form and will converge rapidly for a large value of s. The system of algebraic equations is given in Appendix A.

5.3.3 Crack tip fields

To solve the algebraic equations for temperature and stress fields, we employ the Schmidt method, which is defined in detail in [146]. The temperatures and stress fields can be determined by finding the unknown coefficients $a_n,\ b_n,\ c_n,\ d_n,\ e_n,\ f_n$. Numerical computations are employed to obtain approximate solutions.

Case I: Fully insulated cracks

For a fully insulated crack, the heat flux exhibits square root singularity [150, 151]. The HFIF is a parameter defined to characterise the strength of thermal energy in the medium. HFIF is a physical parameter that is introduced to measure and quantify the thermal energy intensification in the vicinity of the crack tip. In the chapter, at the tips $x = a,\ x = b,\ x = c$ of the cracks, the corresponding HFIF denoted by $K_{Ha},\ K_{Hb},\ K_{Hc}$ have been calculated in the semi-analytical form by mathematical handling of the singularity terms in equations (5.46) and (5.47) as follows.

$$K_{Ha} = k_y^{(1)} \lim_{x \to a+} \sqrt{2(x-a)}\, \frac{\partial T^{(1)}}{\partial y}(x,0) = \frac{\beta_4\ \mu^{(1)}}{\sqrt{\pi\ a}} \sum_{n=1}^{\infty} (-1)^n\ (2n-1)\ b_n, \tag{5.60}$$

$$K_{Hb} = k_y^{(1)} \lim_{x \to b-} \sqrt{2(b-x)}\, \frac{\partial T^{(1)}}{\partial y}(x,h) = \frac{\beta_1\ \mu^{(1)}}{\sqrt{\pi\ (c-b)}} \sum_{n=1}^{\infty} a_n, \tag{5.61}$$

$$K_{Hc} = k_y^{(1)} \lim_{x \to c+} \sqrt{2(x-c)}\, \frac{\partial T^{(1)}}{\partial y}(x,h) = \frac{\beta_1\ \mu^{(1)}}{\sqrt{\pi\ (c-b)}} \sum_{n=1}^{\infty} (-1)^{(n+1)}\ a_n. \tag{5.62}$$

The normalised HFIFs are denoted at each crack tip as $K_{Ha}* = K_{Ha}/q_o\sqrt{a}$, $K_{Hb}* = K_{Hb}/q_o\sqrt{l_o}$, $K_{Hc}* = K_{Hc}/q_o\sqrt{l_o}$ where the normalising factor is the HFIF at the crack tip by considering only a single crack. The dimensionless thermal conductivity $R_c = ah_c/k_y^{(1)}$ is considered to depict the fully permeable and impermeable crack model for the problem.

Case II: Partially insulated cracks

The mode-I SIF at the different cracks' tips is given by

$$K_{Ia} = \lim_{x \to a+} \sqrt{2\pi\ (x-a)}\ \sigma_{yy}^{(1)}(x,0) = \frac{\beta_{16L}}{\sqrt{\pi a}} \sum_{n=1}^{\infty} (-1)^n\ (2n-1)\ f_n, \tag{5.63}$$

$$K_{Ib} = \lim_{x \to b-} \sqrt{2\pi\ (b-x)}\ \sigma_{yy}^{(1)}(x,h) = \frac{\beta_{2L}}{\sqrt{(c-b)}} \sum_{n=1}^{\infty} d_n\ , \tag{5.64}$$

$$K_{Ic} = \lim_{x \to c+} \sqrt{2\pi\ (x-c)}\ \sigma_{yy}^{(1)}(x,h) = \frac{\beta_{2L}}{\sqrt{(c-b)}} \sum_{n=1}^{\infty} (-1)^{n+1}\ d_n. \tag{5.65}$$

Mode-II SIFs at the cracks' tips are given by

$$K_{IIa} = \lim_{x \to a+} \sqrt{2\pi\ (x-a)}\ \sigma_{xy}^{(1)}(x,0) = \frac{\beta_{21L}}{\sqrt{\pi a}} \sum_{n=1}^{\infty} (-1)^n\ 2n\ e_n, \tag{5.66}$$

$$K_{IIb} = \lim_{x \to b-} \sqrt{2\pi\ (b-x)}\ \sigma_{xy}^{(1)}(x,h) = \frac{\beta_{7L}}{\sqrt{(c-b)}} \sum_{n=1}^{\infty} c_n, \tag{5.67}$$

$$K_{IIc} = \lim_{x \to c+} \sqrt{2\pi\ (x-c)}\ \sigma_{xy}^{(1)}(x,h) = \frac{\beta_{7L}}{\sqrt{(c-b)}} \sum_{n=1}^{\infty} (-1)^{n+1}\ c_n. \tag{5.68}$$

Similar to the previous case, the normalised SIFs for mode-I and mode-II can be obtained [133]. The infinite series of equations (5.62)- (5.68) are truncated at finite terms for the numerical computations.

Crack displacements are crucial parameters in fracture failure. The crack faces experience displacement while experiencing deformations. Crack displacements have been categorised as COD in the $y-$ direction and CSD in the $x-$ direction. Displacements have been normalised by the factor $a^2\alpha_{xx}^{(1)}q_0/k_y^{(1)}$.

COD for crack at $y = h$ is defined as

$$v^{(3)}(x,h) - v^{(1)}(x,h), \quad b < x < c. \tag{5.69}$$

CSD for the crack at $y = h$ is defined as

$$u^{(3)}(x, h) - u^{(1)}(x, h), \quad b < x < c. \tag{5.70}$$

A similar procedure is followed for cracks at $y = 0$. The normalised expressions of all parameters above have been plotted graphically to validate their behaviour in different cases in the next section.

Note:

Another type of applied loading could be the in-plane shear, i.e. when the stress component is perpendicular to the crack front but is parallel to the crack surface. For the same considered geometry and mathematical model as depicted in Figure 5.2, consider when the cracks are subjected to shear loading, $p_3(x)$ for all cracks surfaces at $b < x < c$, $-a < x < a$. The boundary and continuity conditions for stresses and displacement fields are similar to the normal loading case. Thus, the

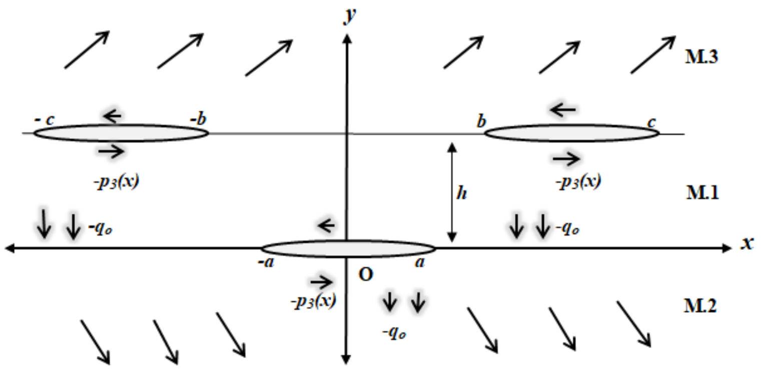

FIGURE 5.2: Geometry of the considered model for in-plane shear.

problem represented by Figure 5.2 can be modeled as

$$\sigma_{yy}^{(1)}(x, h) = 0, \quad \sigma_{xy}^{(1)}(x, h) = -p_3(x) \quad , \quad b < x < c, \tag{5.71}$$

$$\sigma_{yy}^{(1)}(x, 0) = 0, \quad \sigma_{xy}^{(1)}(x, 0) = -p_3(x) \quad , \quad 0 < x < a. \tag{5.72}$$

In addition to the boundary and continuity conditions given in equations (5.24-(5.27) along with the regularity condition is also assumed at infinity.

5.4 Numerical Results and Discussion

This section presents numerical results by selecting certain material choices viz. Tyrannohex, Epoxy and Aluminium alloys [7, 8, 9] for the considered problem as shown in Table 5.1. The normalised temperatures, HFIFs, SIFs for mode-I and mode-II, COD, and CSD are calculated for different particular cases and displayed graphically after validating the accuracy of the series solution. The static heat flux q_o flows in the downward direction, and for the numerical computations of the problem, the mechanical loads $p_1 = p_2 = 300$ MPa have been considered.

5.4.1 Validity of numerical computation

For numerical computations and for the sake of mathematical ease, the infinite series involved in expressions of parameters in the previous section is truncated for $n = 5$. The validity of this truncation has been justified through Table 5.2 and Table 5.3. In the context of temperature field algebraic equations, it has been demonstrated through the aforementioned tables that the algebraic system's left-hand side and right-hand side in equations (5.51) and (5.52) exhibit close proximity. This concludes that the left side of equations (5.51) and (5.52) with infinite series containing the unknown coefficient terms in which the approximate solution of the problem is dependent are in agreement with the right side expression of the same equations, respectively, which is an exact value dependent on some material parameters. For different values of n, Table 5.4 depicts the values of approximate solutions. The numerical computations were performed using the MATHEMATICA software, employing the Schmidt method outlined in sub-section 1.7.2.

5.4.2 Validation of the methodology

In Figure 5.3, a comparison study of q_{oc}/q_o between the present method and the explicit form solution in [8] is presented for two cases viz. $R_c = 1.0$ and $R_c = 2.0$. Wu et al. [8], in their study, have worked on embedded cracks in an orthotropic medium under quadratic thermal and mechanical loadings. For the purpose of comparison, the present problem has been reduced to the particular case of an orthotropic medium with the single crack of length $2a$ present at $y = 0$. The results reveal the dependency of thermal resistance. The quadratic loading terms have been neglected to validate the present study, and graphs have been plotted for constant values. For material choice, namely, Tyrannohex, both studies show similar behaviour for different values of x/a for central crack. Absolute values have been plotted to account for the opposite direction of applied forces in both studies. The difference in values at some points can be attributed to the different methodologies used in both the works and the number of truncated series considered for the present chapter. Figure 5.5 is plotted for the present study for different values of x/a while, for increasing ratio, normalised heat flux increases. A comparison study with another kind of model called the thermal medium model has been conducted for the case of central crack is shown in Figure 5.4, and it exhibits a similar behaviour for q_{oc}/q_c as shown in a previous study by Zhong and Wu [6]. The plot is drawn to show the variations of normalised heat flux vs ratio h_c/k_y. In both studies, it can be seen that as the ratio of thermal conductivity increases, the normalised heat flux q_{oc}/q_c also increases, and it has been verified that q_0 is the limiting value for q_{oc}. The plot reveals the comparative study between two models, namely the thermally conducting model that has been utilised in the present study and the thermal medium model.

5.4.3 Discussion

The relationship between heat flux, the thermal conductivity of crack region, and crack lengths are illustrated in Figures 5.6-5.11. Different material parameters have been chosen to plot the graphs to draw the variations in heat flux and thermal resistance for partially insulated cracks inside the crack regions. The condition $R_c = 0$ signifies a thermally impermeable crack model. As the value of R_c increases, the thermal conductivity of the crack region within the crack also increases, surpassing that of the crack's exterior for $R_c > 1$. Graphs are constructed for crack lengths $(c-b)/2a = 1.0$ and strip width $h/2a = 0.5$. The Figures 5.6, 5.7 and 5.11 illustrate the two-dimensional and three-dimensional plots showcasing the relationship between the dimensionless heat flux q_{oc}/q_o and the non-dimensional thermal conductivity of crack region R_c at various distances from the crack tip $x = a$ within the central crack. It is evident from these plots that as the value of R_c increases and as we move toward the centre of the crack region, the dimensionless heat flux q_{oc} increases. For the upper crack region between the crack tips $x = b$, $x = c$, the Figure 5.8, Figure 5.9, and Figure 5.10 depicts the plots for q_{oc}/q_o vs. R_c for different points in crack region. From these plots, there is an observed distinction in the behaviours of the two cracks, which lies in their response to variations in the thermal conductivity of the crack region. Specifically, the upper crack demonstrates a decline in heat flux values at the centre of the crack when subjected to the higher thermal conductivity of the crack region. Conversely, the central fracture exhibits the highest peak value of heat flux precisely at $x/a = 0$. These figures help better understand and analyse the thermal flux for the considered conducting crack model and how the cracks behave distinctly under the same conditions.

Figures 5.13 and 5.12 display the absolute values of temperature differences for all cracks. As the thermal conductivity (h_c) increases, there is a corresponding decrease in the temperature difference. This relationship can be explained by the fact that as the thermal conductivity of the crack region increases, the temperature difference between the upper and lower regions becomes smaller. The temperature difference diminishes as the level of thermal permeability increases for a particular crack. The results are in agreement with the analytical findings of [133]. These figures have helped in analysing the variations in temperatures across the interface due to the presence of cracks and the effect of their thermal conductivity on the temperature change.

Figure 5.14 illustrates the graph representing the normalised HFIF at the crack tip $x = a$. The crack under consideration is insulated, denoted by $q_{oc} = 0$, and the non-dimensional strip width is fixed at $h/2a = 0.5$ with a uniform heat flow of q_0 in the downward direction. Curves of varying crack length ratios $(c-b)/2a$ are plotted for the selected material options. It can be noted that when $(2a+c-b)/2(a+c) < 0.5$, there is an increase in the HFIF as the crack length ratio grows. However, this trend is reversed when overlapping of cracks occurs, as increasing crack length ratios lead to a decrease in HFIF. Figure 5.15 illustrates the graph representing the normalised HFIF at the crack tip $x = a$ when it is insulated, i.e. $q_{oc} = 0$. The graph is plotted using different non-dimensional strip width $h/2a$. The crack length ratio, $(c-b)/2a$, is 1.0 for the selected material options. It is evident that in the case when the ratio $(2a+c-b)/2(a+c)$ is less than 0.5 and the strip width is equal to or smaller than the length of the central crack, HFIF experiences a decrease followed by a progressive increase. Conversely, when the ratio $h/2a$ is more than 0.5, the HFIF initially increases and subsequently falls. Moreover, it is observed that as the ratio $h/2a$ increases, the value of HFIF decreases. Figure 5.16 illustrates the graph representing the normalised HFIF at the crack tip $x = b$ for a fully insulated crack. The non-dimensional strip width is maintained at a fixed value of $h/2a = 0.5$. According to the chosen materials, curves are plotted for various crack length ratios, namely $(c - b)/2a$. The relationship between the crack length ratio and HFIF has a positive correlation, whereby a corresponding increase in HFIF accompanies an increase in the crack length ratio. Figure 5.17 illustrates the graph representing the normalised HFIF at the crack tip $x = b$. The graph considers an insulated crack and plots several curves based on the non-dimensional strip width $h/2a$. The crack length ratio, $(c - b)/2a$, is 1.0 for the selected materials. The data reveals a noticeable decline in HFIF, followed by a steady resurgence in its behaviour. Also, it can be observed that as $h/2a$ increases, HFIF decreases. Figure 5.18 depicts the graph for normalised HFIF at crack tip $x = c$ for a completely insulated crack and non-dimensional strip width $h/2a = 0.5$. Different curves are plotted for different values of crack length ratios $(c - b)/2a$ for the considered material choices. It can be observed that as the crack length ratio increases, HFIF also increases. Figure 5.19 depicts the graph for normalised HFIF at crack tip $x = c$ for a completely insulated crack and non-dimensional strip width $h/2a$. Here, the crack length ratio is $(c-b)/2a = 1.0$. It can be observed that HFIF decreases and then gradually starts increasing behaviour. It can be observed that as $h/2a$ increases, HFIF decreases. The values of HFIF at $x = c$ are slightly less than the HFIF at $x = b$, as seen in Figures 5.16, 5.17, 5.18 and 5.19. These plots illustrate the relationship between heat flux intensity, crack lengths, and strip width in an insulated crack model where the crack region has no conductivity of its own. Additionally, it highlights that the highest values for heat flux intensity occur at the crack tip $x = b$.

A detailed analysis of the thermal conductivity, $k^{(i)}$ on the HFIF, has been conducted in the next few plots. Figures 5.20, 5.21 and 5.22 represent the plots of HFIF for different ratios of thermal conductivity between three materials keeping $(c-b)/2a = 1.0$ and $h/2a = 0.5$ as fixed. Based on these ratios, five different cases: (I) when all materials are dissimilar orthotropic materials, (II) all isotropic materials and medium M.2 are identical with medium M.3, (III) all orthotropic materials and M.2 are identical with M.3, (IV) all similar orthotropic material choices and (V) all similar isotropic materials, have been considered and the graphs are plotted for each case given in Table 5.5. It is observed that the HFIF at crack tip $x = b$ is slightly more than the HFIF at crack tip $x = c$, as seen in Figures 5.21 and 5.22, but both crack tips show similar kinds of behaviour for each case. The values for case (III) are nearly the same as cases (IV) and (V), whereas cases (IV) and (V) show the same values at $x = b$ and $x = c$, but significant differences are found at $x = a$. For crack tip $x = a$ in Figure 5.20, cases (III) and (IV) have the same values of HFIF. A similar kind of analysis has been carried out in [134]. These plots reveal the relation between different kinds of materials based on thermal conductivity coefficients and the corresponding variations in heat flux. The HFIF is a measure of thermal energy intensification near the crack tips. The same variations for different combinations of material properties are shown graphically in Figures 5.21 and 5.22. In the case of dissimilar orthotropic media, the HFIF depends on relative ratio k_y/k_x. Generally, the isotropic material possesses less value of HFIF under the same loading conditions as seen in Figure 5.20.

Stresses induced by thermal loading and heat flux effects have been studied in the current problem through various plots. SIFs at all crack tips have been plotted for constant normal tensile load values for cracks under thermal and mechanical loadings. Figures 5.23-5.34 illustrate the plots of normalised SIF at all crack tips for various strip width ratios. In these cases, the crack length ratio is maintained at a constant value of $(c-b)/2a = 0.5$. Various scenarios are examined by considering different values of $h/2a = 0.2,\ 0.3,\ 0.5$ while considering different values of the partial conductivity coefficient $h_c = 0.0,\ 0.5$. The graphs depicting the SIF for modes I and II have been generated for the identical scenarios. The adjacent graphs illustrate the impact of the partial insulation coefficient on the SIF at the tips of cracks. The SIF decreases as the thermal conduction increases, as evidenced by the SIF curves for mode-I and mode-II. In all cases, it is noted that the SIF decreases with an increase in the thermal conductivity parameter. The SIF increases as the strip width ratio increases. Hence, the influence of the thermal conductivity coefficient and strip width on the SIF becomes evident. Figure 5.23 and Figure 5.24 illustrate the graphical representations of the normalised SIF for mode-I as a function of $(2a+c-b)/2(a+c)$ at the crack tip located at $x = a$. Multiple curves represent the NSIF values for various strip widths for $h_c = 0$ and $h_c = 0.5$. The SIFs for mode-I at crack tips $x = b$, $x = c$ are illustrated in Figures 5.25, 5.26, 5.27, and 5.28. Multiple curves represent the NSIF values for varying strip width at two values, $h_c = 0$ and $h_c = 0.5$. Figures 5.29 and 5.30 illustrate the graphs representing the normalised SIF of mode-II as a function of $(2a+c-b)/2(a+c)$ at the crack tip $x = a$. The values of NSIF for various strip width are shown for $h_c = 0$ and $h_c = 0.5$. Likewise, mode II NSIF at crack points $x = b$ and $x = c$ are illustrated in Figures 5.31, 5.32, 5.33, and 5.34. Multiple curves represent the NSIF values for various strip width for $h_c = 0$ and $h_c = 0.5$. The impact of the thermal conductivity coefficient on stresses is justified through these graphs. The results successfully reveal that with an increase in thermal conductivity value, there are significant decreases in the SIFs.

Next, the aim is to show the effect of heat conduction on the COD, as seen in Figures 5.35, 5.36, 5.37 and 5.38. NCOD decreases with an increase in h_c for a given fixed crack length ratio and a given strip width ratio. NCOD vanishes near the crack tips and reaches a peak value at the centre of the upper crack. In Figures 5.39 and 5.40, the normalised CSD is plotted for the upper and central cracks. It can be observed that the NCSD is symmetric for $b < x < c$ and vanishes at its crack tips $x = b$ and$x = c$. But it is non-symmetric for the central crack $0 < x < a$ and vanishes at the crack tip $x = a$. The phenomena are shown for different values of $h/2a$, keeping the crack lengths fixed and $h_c = 0.5$. Crack displacements are important fracture parameters for the analysis of plastic deformations. The numerical results depicted for COD and CSD reveal the impact of thermal and mechanical loadings.

5.5 Conclusion

In conclusion, the investigation of crack behaviour in orthotropic composite materials with partially insulated cracks, subject to a uniform heat flux q_o in the negative y-axis direction and tensile stress applied to the crack surfaces, has been conducted. The present chapter formulates the governing equations and the required boundary and continuity conditions for both temperature fields and stresses for the model under consideration. Fourier transforms, and their corresponding inverses have been employed to convert the problem into systems of algebraic equations by leveraging the orthogonality property of Chebyshev-like polynomials. The Schmidt method is used to solve the algebraic equations containing unknown coefficients. These equations are then utilised to determine the temperature and stress fields completely.

As a result, we delve into the analysis of thermal conductivity within cracks, exploring the interconnections of various parameters. Determining the HFIF, mode-I and mode-II SIFs, COD, and CSD enhances the ability to analyse the dependency of crack lengths, bonded strip width, and thermal conduction coefficient on these parameters. Utilising semi-analytical methods and numerical computations, the expressions of various physical parameters have been calculated and visually depicted their relationship for specific material selections. Notably, it has been found that the partial insulation coefficient of the crack surface significantly influences the temperatures, SIF, COD, and CSD. The comprehensive results and discussions shed light on this intricate subject, offering a thorough exploration. As the thermal conductivity coefficient increases, the temperature difference tends to zero. Graphs clearly depict that the numerical values of SIF are higher in the case of mode-I fracture as compared to the mode-II cracks.

Moreover, a comparative study has been conducted, providing an insightful analysis of the present methodology in comparison to the previous study. The similarities observed in the nature of curves in both studies further agree with the robustness of the findings.

Materials	E_{xx}(GPa)	E_{yy}(GPa)	G_{xy}(GPa)	$\alpha_{xx}(10^{-6}\mathrm{K}^{-1})$	$\alpha_{yy}(10^{-6}\mathrm{K}^{-1})$
Tyrannohex	135	87	50	3.2	3.2
Epoxy	3.45	3.45	1.28	64.3	64.3
Aluminium alloy	90.43	116.36	38.21	8.0	3.78
Materials	ν_{xy}	ν_{yx}	k(W/mK)	μ(W/mK)	
Tyrannohex	0.15	0.097	1.046	2.941	
Epoxy	0.35	0.35	0.18	0.18	
Aluminium alloy	0.28	0.28	0.844	25.173	

TABLE 5.1: Properties for the considered materials [7, 8, 9].

x/l_o	$(\sum_{n=1}^{\infty} a_n E_{1n}(x) + \sum_{n=1}^{\infty} b_n E_{2n}(x))/q_o\sqrt{l_o}$	$h_{1n}(x)/q_o\sqrt{l_o}$	Absolute error
0.10000	-0.010606+0.0000 i	-0.01082+0.0000 i	2.1×10^{-4}
0.11111	-0.01059+0.0000 i	-0.01081+0.0000 i	2.2×10^{-4}
0.50000	-0.009349+0.0000 i	-0.00942+0.0000 i	7.1×10^{-5}
0.92857	-0.004135+0.0000 i	-0.00403+0.0000 i	1.0×10^{-4}
0.99999	-0.0000501+0.0000 i	-0.000048+0.0000 i	2.1×10^{-6}

TABLE 5.2: Error analysis of values of approximate series (LHS) and exact values of RHS in equations (5.51) for $(c-b)/2a = l_o/a = 0.5$, $h/2a = 0.5$.

****

x/a	$(\sum_{n=1}^{\infty} a_n E_{3n}(x) + \sum_{n=1}^{\infty} b_n E_{4n}(x))/q_o\sqrt{a}$	$h_{2n}(x)/q_o\sqrt{a}$	Absolute error
0.10000	-0.06522+0.0000 i	-0.06281+0.0000 i	2.4×10^{-3}
0.11111	-0.06475+0.0000 i	-0.06242+0.0000 i	2.3×10^{-3}
0.50000	-0.04502+0.0000 i	-0.04681+0.0000 i	1.7×10^{-3}
0.92857	-0.017413+0.0000 i	-0.01769+0.0000 i	2.7×10^{-4}
0.99999	-0.000216+0.0000 i	-0.000020+0.0000 i	1.6×10^{-5}

Table 5.3: Error analysis of values of approximate series (LHS) and exact values of RHS in equations (5.52) for $(c-b)/2a = l_o/a = 0.5$, $h/2a = 0.5$.

n	x/l_o	Absolute error
3	0.10000	1.1×10^{-4}
	0.50000	9.4×10^{-5}
	0.99999	0.1×10^{-6}
4	0.10000	1.8×10^{-4}
	0.50000	1.5×10^{-4}
	0.99999	4.2×10^{-5}
5	0.10000	2.1×10^{-4}
	0.50000	7.1×10^{-5}
	0.99999	2.1×10^{-6}

Table 5.4: Error analysis for different values of truncated terms n for (5.51) when $(c-b)/2a = l_o/a = 0.5$, $h/2a = 0.5$.

Cases	$k^{(1)}$	$k^{(2)}$	$k^{(3)}$	$k_x^{(2)}/k_x^{(1)}$	$k_x^{(3)}/k_x^{(1)}$
(I)	1	2	3	3	2
(II)	1	1	1	5	5
(III)	5	5	5	5	5
(IV)	5	5	5	1	1
(V)	1	1	1	1	1

Table 5.5: Different cases based on thermal conductivity coefficient.

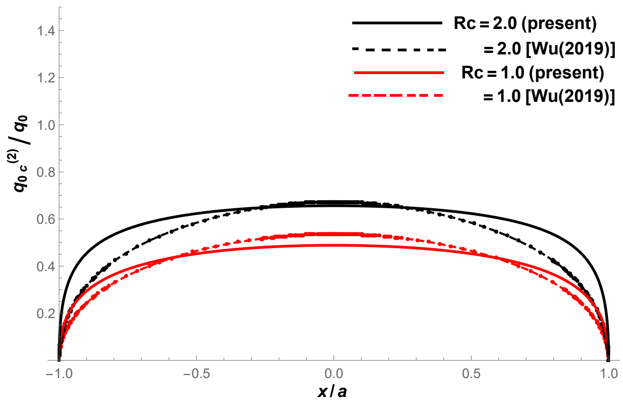

FIGURE 5.3: Plots of q_{oc}/q_o vs x/a when only central crack is considered in orthotropic plane.

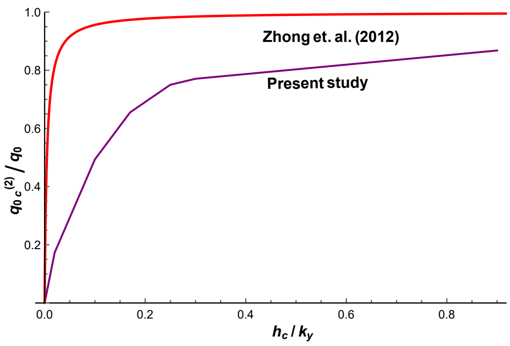

FIGURE 5.4: Comparative study between thermal medium model [6] and thermal conducting model for present study by fixing $(c-b)/2a = 0.0,\ h/2a = 0.5$.

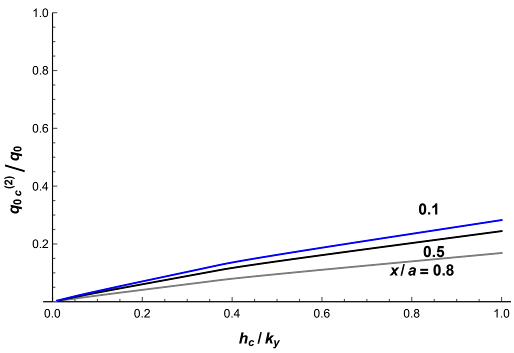

FIGURE 5.5: Plots of dimensionless heat flux q_{oc}/q_o for central crack vs thermal conductivity h_c by fixing $(c-b)/2a = 0.0,\ h/2a = 0.5$.

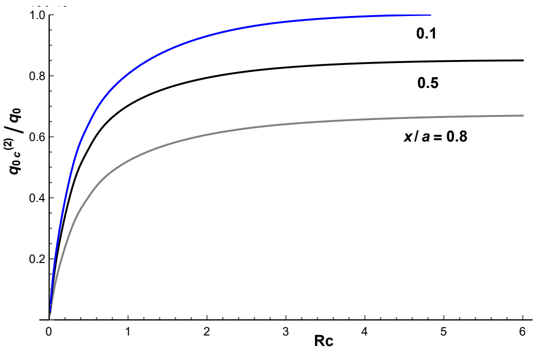

FIGURE 5.6: Plots of Dimensionless heat flux q_{oc}/q_o for central crack vs non-dimensional thermal conductivity R_c by fixing $(c-b)/2a = 1.0,\ h/2a = 0.5$

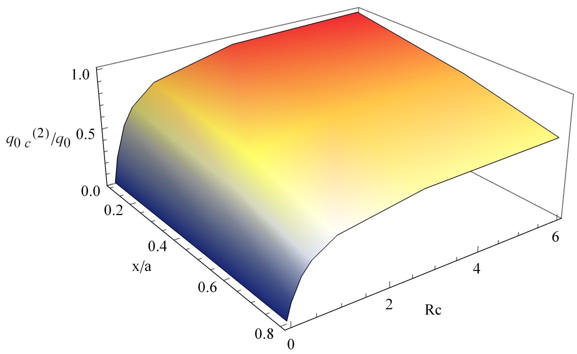

FIGURE 5.7: 3-D plot for heat flux vs dimensional thermal conductivity R_c vs x/a by fixing $(c-b)/2a = 1.0,\ h/2a = 0.5$

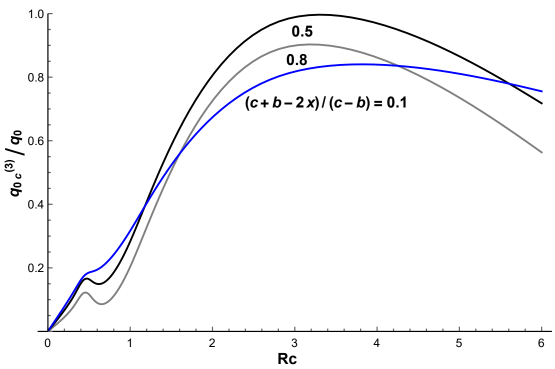

FIGURE 5.8: Plots of Dimensionless heat flux q_{oc}/q_o for upper crack vs non-dimensional thermal conductivity R_c by fixing $(c-b)/2a = 1.0,\ h/2a = 0.5$

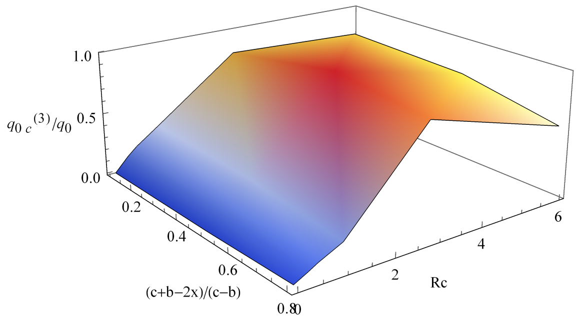

FIGURE 5.9: 3-D plot vs dimensional thermal conductivity R_c vs x/a by fixing $(c-b)/2a = 1.0,\ h/2a = 0.5$.

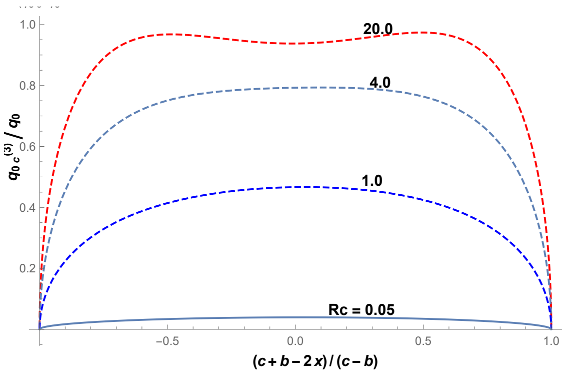

FIGURE 5.10: Plots of Dimensionless heat flux q_{oc}/q_o for upper crack vs $(c+b-2x)/(c-b)$ for different values of non-dimensional thermal conductivity R_c.

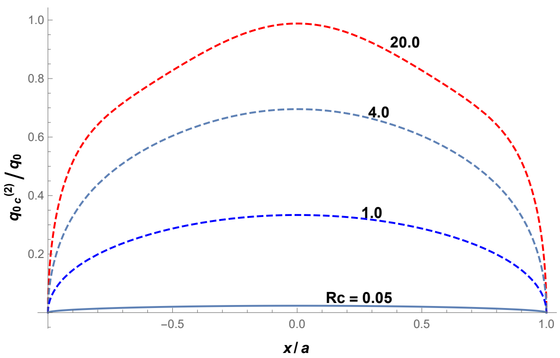

FIGURE 5.11: The plot of Dimensionless heat flux q_{oc}/q_o for upper crack vs x/a for different values of non-dimensional thermal conductivity R_c.

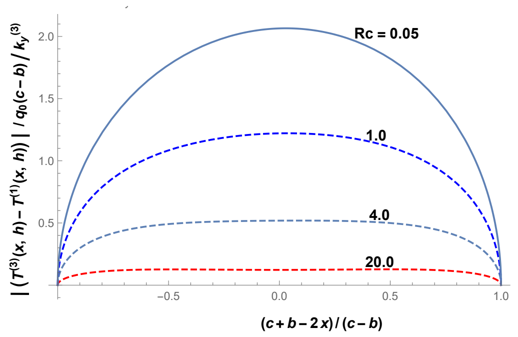

FIGURE 5.12: Plots of normalised temperature difference for different values of R_c for upper crack $b < x < c$.

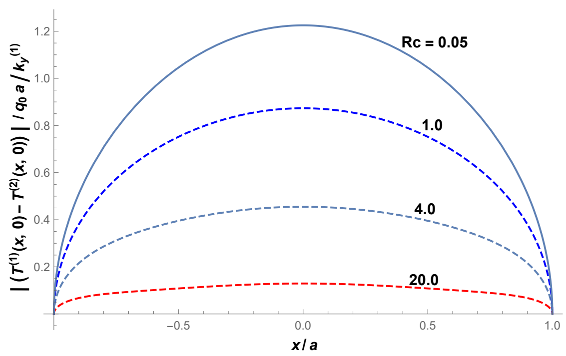

FIGURE 5.13: Plots of normalised temperature difference for different values of R_c for $0 < x < a$.

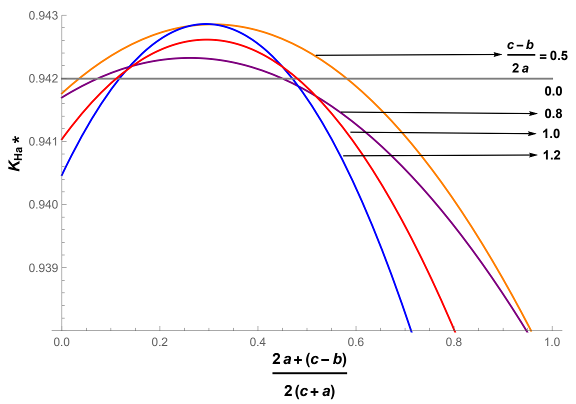

FIGURE 5.14: Plots of Normalised Heat flux intensity factor at crack tip $x = a$ for different crack length ratios $(c - b)/2a$.

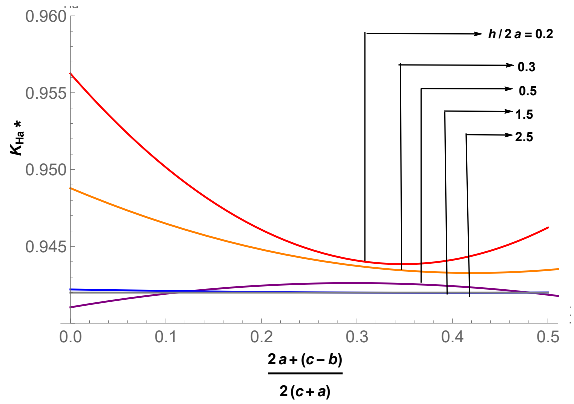

FIGURE 5.15: Plots of Normalised Heat flux intensity factor at crack tip $x = a$ for different strip width ratios $h/2a$.

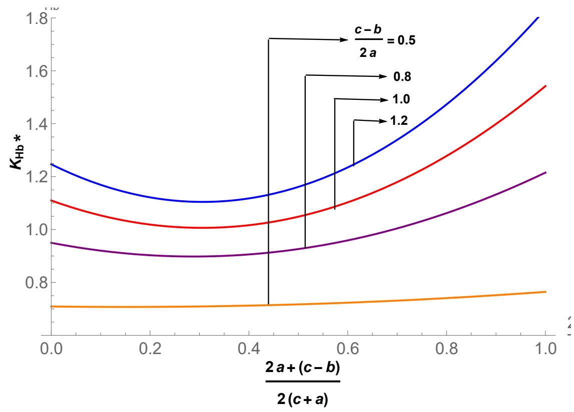

FIGURE 5.16: Plots of Normalised Heat flux intensity factor at crack tip $x = b$ for different crack length ratios $(c - b)/2a$.

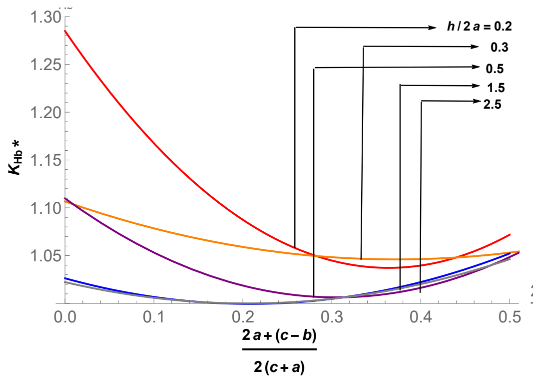

FIGURE 5.17: Plots of Normalised Heat flux intensity factor at crack tip $x = b$ for different strip width ratios $h/2a$.

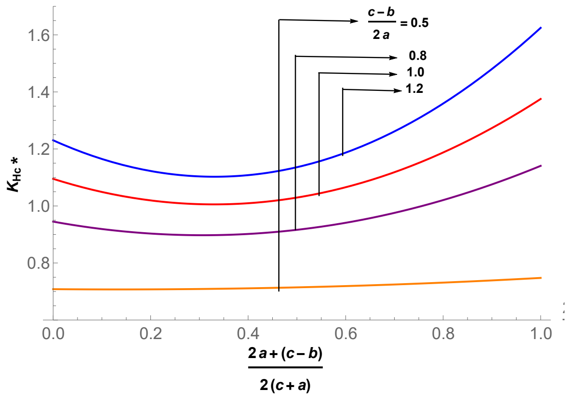

FIGURE 5.18: Plots of Normalised Heat flux intensity factor at crack tip $x = c$ for different crack length ratios $(c - b)/2a$.

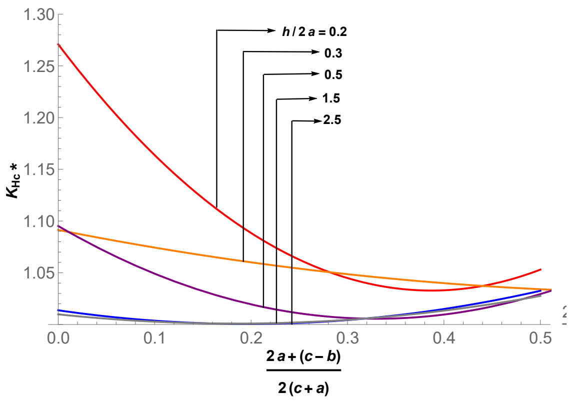

FIGURE 5.19: Plots of Normalised Heat flux intensity factor at crack tip $x = c$ for different strip width ratios $h/2a$.

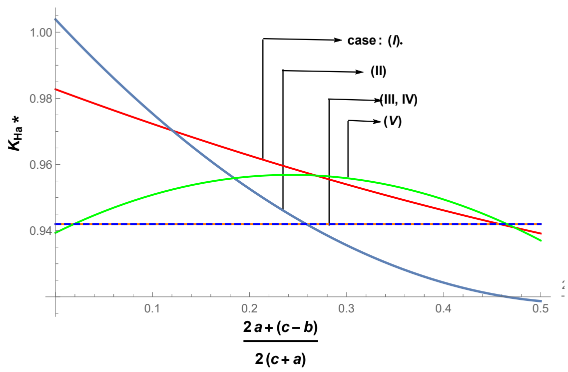

FIGURE 5.20: Plots of Normalised Heat flux intensity factor at crack tip $x = a$ for different thermal conductivity coefficient ratios for different materials.

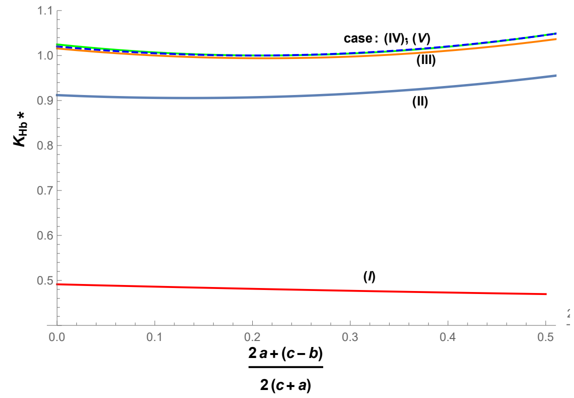

FIGURE 5.21: Plots of normalised heat flux intensity factor for different thermal conductivity coefficient ratios for different materials for $x = b$.

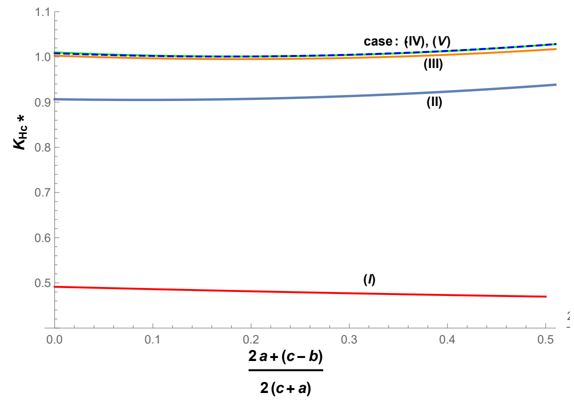

FIGURE 5.22: Plots of normalised heat flux intensity factor for different thermal conductivity coefficient ratios for different materials for $x = c$.

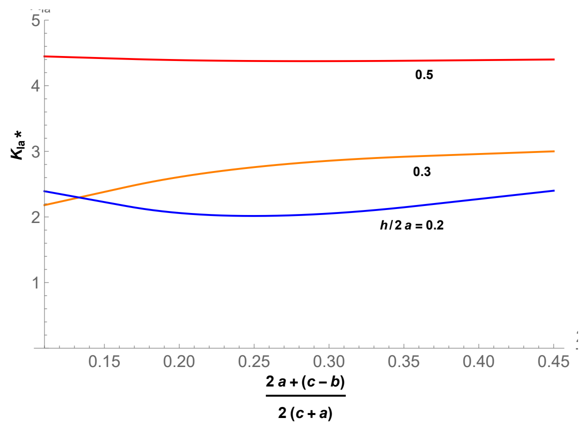

FIGURE 5.23: Plots of normalised stress intensity factor of mode-I at crack tip $x = a$ for different $h/2a$ when $h_c = 0.0$.

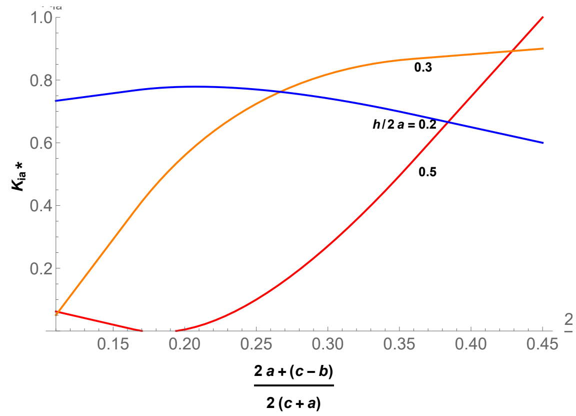

FIGURE 5.24: Plots of normalised stress intensity factor of mode-I at crack tip $x = a$ for different $h/2a$ when $h_c = 0.5$.

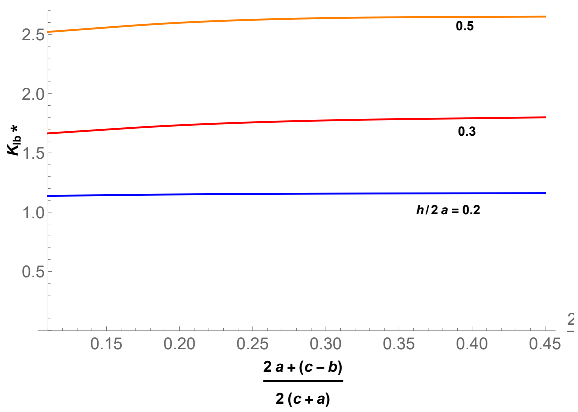

FIGURE 5.25: Plots of normalised stress intensity factor of mode-I at crack tip $x = b$ for different $h/2a$ when $h_c = 0.0$.

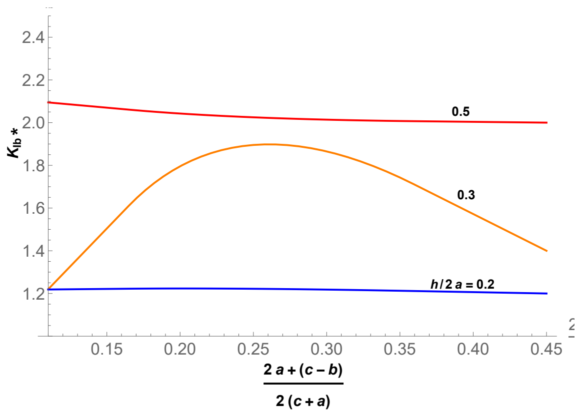

FIGURE 5.26: Plots of normalised stress intensity factor of mode-I at crack tip $x = b$ for different $h/2a$ when $h_c = 0.5$.

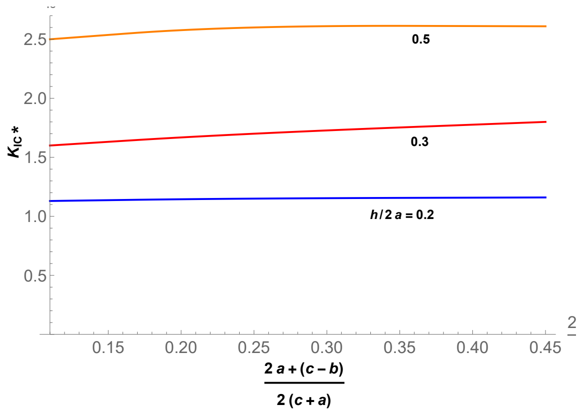

FIGURE 5.27: Plots of normalised stress intensity factor of mode-I at crack tip $x = c$ for different $h/2a$ when $h_c = 0.0$.

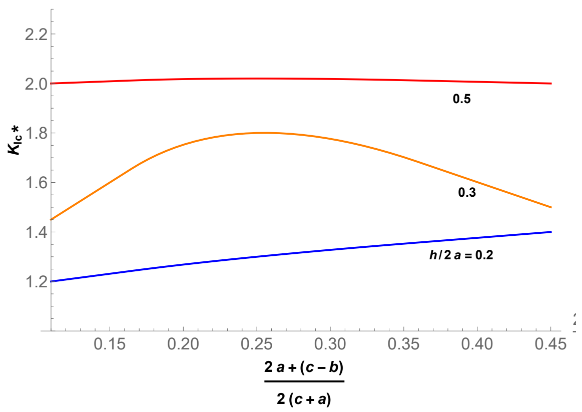

FIGURE 5.28: Plots of normalised stress intensity factor of mode-I at crack tip $x = c$ for different $h/2a$ when $h_c = 0.5$.

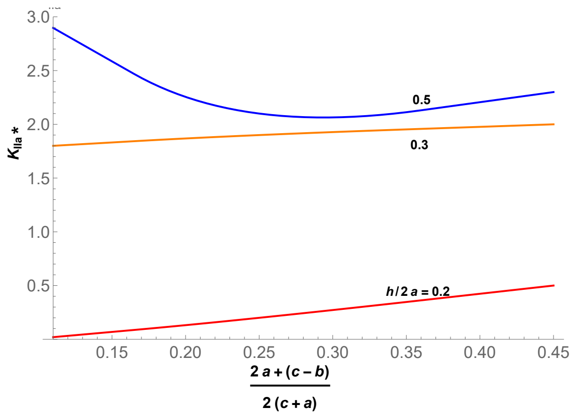

FIGURE 5.29: Plots of normalised stress intensity factor of mode-II at crack tip $x = a$ for different $h/2a$ when $h_c = 0.0$.

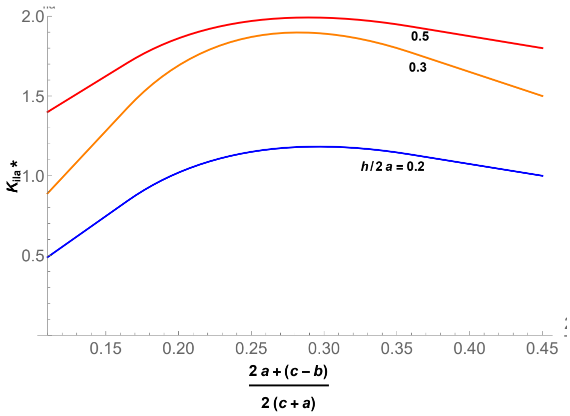

FIGURE 5.30: Plots of normalised stress intensity factor of mode-II at crack tip $x = a$ for different $h/2a$ when $h_c = 0.5$.

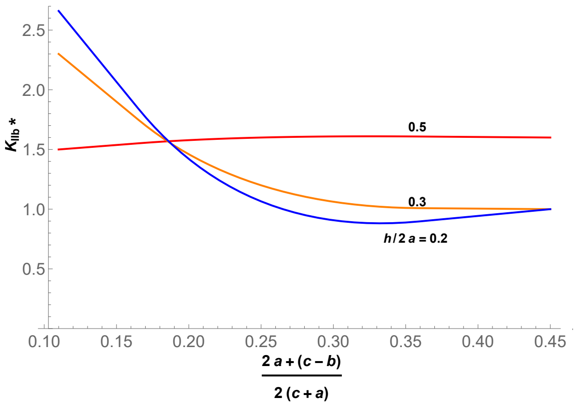

FIGURE 5.31: Plots of normalised stress intensity factor of mode-II at crack tip $x = b$ for different $h/2a$ when $h_c = 0.0$.

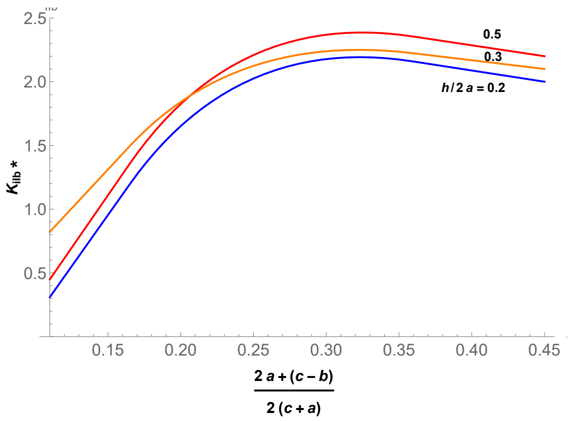

FIGURE 5.32: Plots of normalised stress intensity factor of mode-II at crack tip $x = b$ for different $h/2a$ when $h_c = 0.5$.

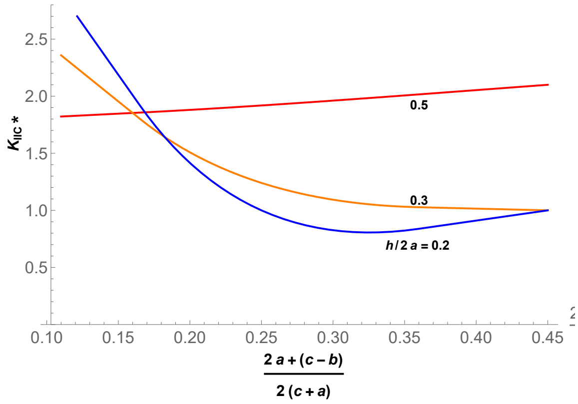

FIGURE 5.33: Plots of normalised stress intensity factor of mode-II at crack tip $x = c$ for different $h/2a$ when $h_c = 0.0$.

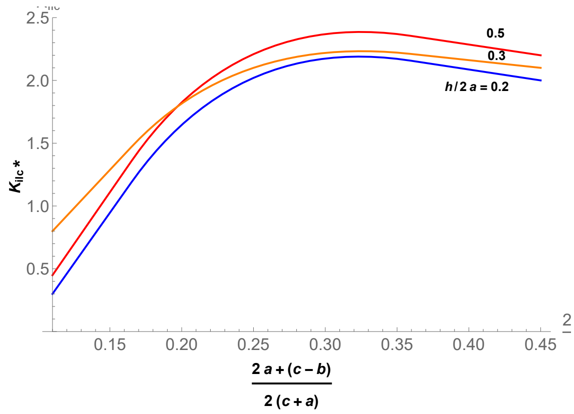

FIGURE 5.34: Plots of normalised stress intensity factor of mode-II at crack tip $x = c$ for different $h/2a$ when $h_c = 0.5$.

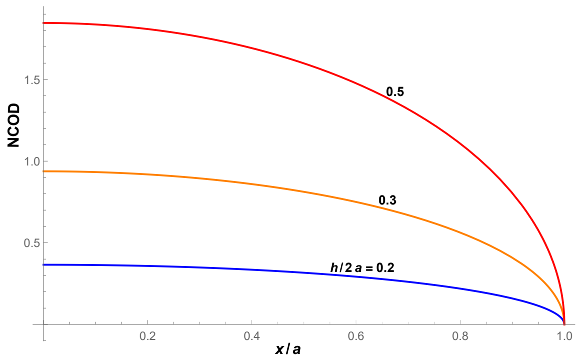

FIGURE 5.35: Plots of normalised opening displacement of crack at crack tip $x = a$ for different $h/2a$ when $h_c = 0.0$.

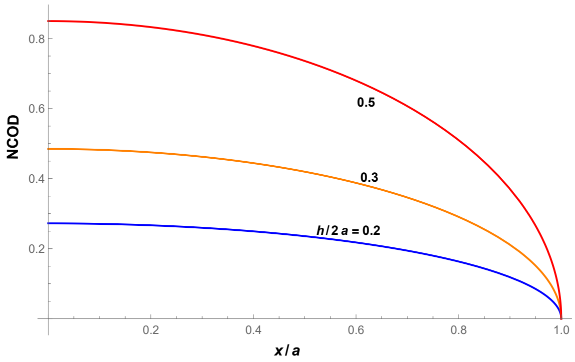

FIGURE 5.36: Plots of normalised opening displacement of crack at crack tip $x = a$ for different $h/2a$ when $h_c = 0.5$.

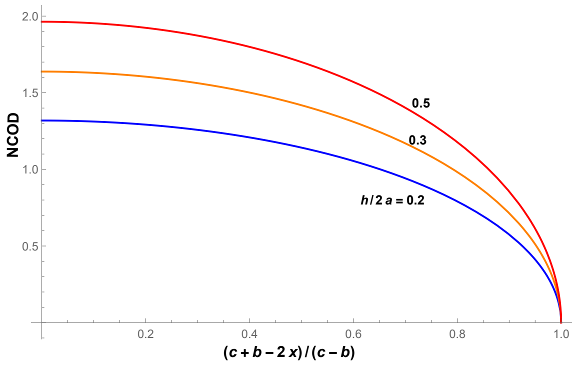

FIGURE 5.37: Plots of normalised opening displacement of crack at crack tip $x = b$ and $x = c$ for different $h/2a$ when $h_c = 0.0$

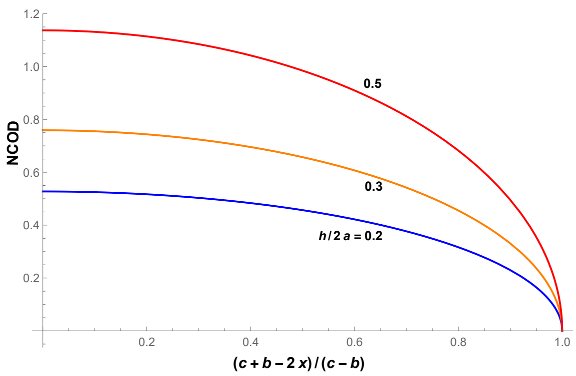

FIGURE 5.38: Plots of normalised opening displacement of crack at crack tip $x = b$ and $x = c$ for different $h/2a$ when $h_c = 0.5$.

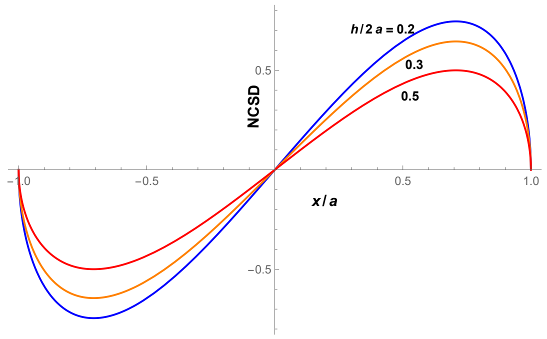

FIGURE 5.39: Plots of normalised sliding displacement of crack for different $h/2a$ tip $x = a$

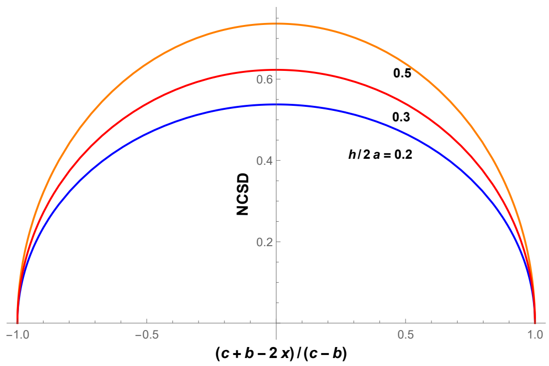

FIGURE 5.40: Plots of normalised sliding displacement of crack for different $h/2a$ tip $x = b$ and $x = c$.